Strong Attractions and Repulsions Mediated by Monovalent Salts

Supporting Information Appendix

Yaohua Li[1], Martin Girard[1], Meng Shen[1], Jaime Andres Millan[1], and Monica Olvera de la Cruz[1,2,3]

[1] Department of Materials Science and Engineering, [2] Department of Chemistry, Department of Physics and Astronomy, Northwestern University, Evanston Il 60208

1. Atomistic Simulations

1.1 Radial Distribution Functions

The ion-ion radial distribution functions used in the Iterative Boltzmann Inversion (see main text and the section 2 of this SI Appendix) are calculated from atomistic simulations of NaCl-water solutions. Periodic boundary conditions (PBC) are applied on the x-, y- and z- dimensions of a 5 nm × 5 nm × 5 nm simulation box. NaCl concentrations from 0.3 M to 1 M are simulated. The number of water molecules in the simulation box range from 4131 to 3575 depending on NaCl concentration. Particle Mesh Ewald (PME) method (1) is applied to treat the electrostatic interaction beyond the cutoff of 1.2 nm. The simulation timestep is 1 fs. The systems are equilibrated at a constant pressure of 1 atm for 5 ns before collecting data. Two water models are studied: the TIP3P model and SPC/E model. The systems with TIP3P water model are simulated using NAMD (2) which is optimized for TIP3P water model, and the systems with SPC/E are simulated using GROMACS (3).

RDFs are calculated from simulation trajectories of over 2 million MD steps using the RDF extension of Visual Molecular Dynamics (VMD) (4). The models for Na^+ and Cl^- in the majority of the all-atomistic simulations are compatible with the TIP3P water model (5) and reproduce experimental osmotic pressures up to 5 M salt concentration (6). Na^+ and Cl^- models that are compatible with SPC/E water model (7) and reproduce experimental osmotic pressures up to 4 M salt concentration have also been reported (8, 9). For consistency, all coarse-grained results in the main text are simulated using potentials derived from the TIP3P water model. A brief discussion about the difference in dielectric constant and resulting NP-NP interactions introduced by the two water model is given in the next section.

1.2 Calculation of the Solvent Dielectric Constant

The dependence of the dielectric constant on NaCl concentration is calculated from the fluctuations of the total dipole moments of water molecules in atomistic simulations (10), and shown in Fig. S1. The dielectric constant decreases with the increase of salt concentration, because more water molecules are replaced by ions. In general, the SPC/E water model reproduces the experimental dielectric constant more closely (11), while the TIP3P water model consistently overestimates the dielectric constant (12), but ion-ion correlation is parameterized in a wider concentration range for TIP3P model. The SPC/E water model also captures the long-range electrostatic interactions more accurately. Since our purpose is to derive the short-range interaction of ions, either model is acceptable. In fact, we observe similar potentials of mean force between nanoparticles regardless of the water model used when calculating the ion-ion correlations

(Fig. S2), suggesting that both the TIP3P and SPC/E water models capture the solvent mediated correlation effects in our atomistic simulations. In most of the coarse-grained simulations we use the dielectric constants and ion pair correlation function calculated from TIP3P water model.

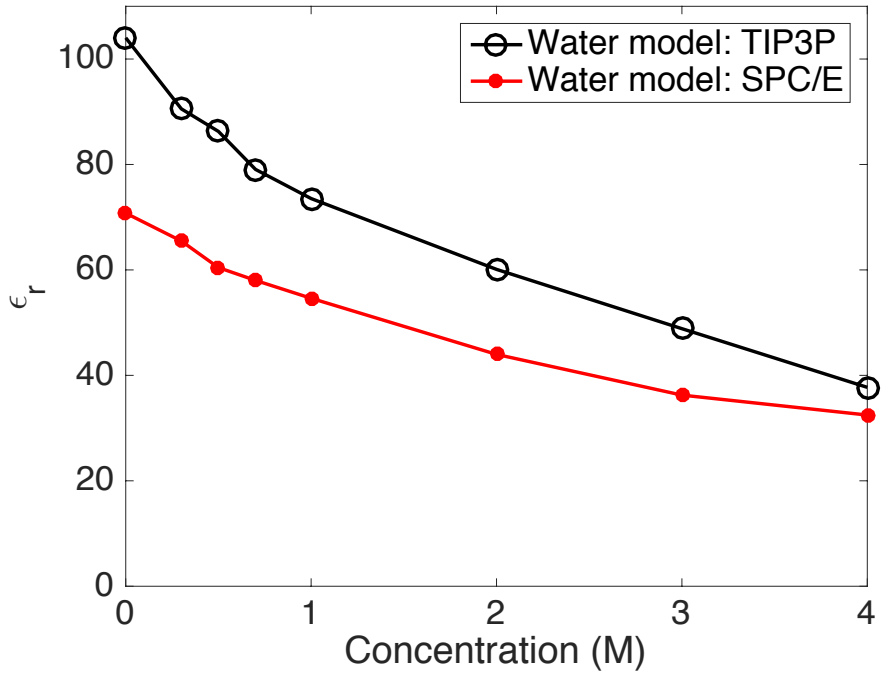

Fig. S1 Dielectric constant value vs. NaCl concentration using the TIP3P water model (open circles) and SPC/E water model (filled circles).

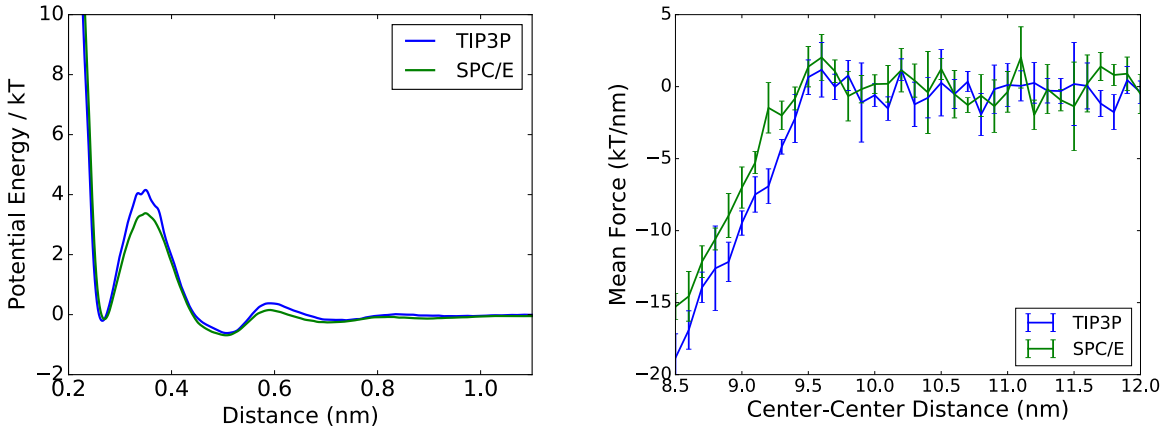

Fig. S2 Comparison of coarse-grained Na-Cl ion potential derived from two water models (a) and comparison of NP-NP interaction using the two coarse grained potential (b) for 1M NaCl and neutral NPs.

2. Derivation of the Coarse-grained Inter-Ion Potential

We develop a coarse-grained salt solution model with an implicit solvent based on the radial distribution functions (RDF) for ions. The method used to calculate effective interaction potentials between ions from RDFs was proposed by Lyubartsev et al. in (13) using Monte Carlo simulations. Here we extended the method for the case of high ionic strength by introducing a salt concentration-dependent dielectric constant (9, 14), which decrease significantly from pure water. To capture this effect, we calculated a concentration-dependent dielectric constant from the fluctuation of water dipoles by all-atomistic simulations, and used it in the long-range Coulomb potential. The short-range part of the effective potential between ions are represented by a tabulated potential calculated via the Iterative Boltzmann Inversion (IBI) method described in ref (13, 15), and the long-range electrostatic interactions are calculated by Particle-Particle Particle-Mesh Ewald Sum (PPPM) implemented in HOOMD-blue (1, 16). In the IBI method, the effective potential $U(r)$ between ions is modified iteratively by the formula,

$$U_{i+1} = U_i(r) - k_B T \log\left(\frac{g_i(r)}{g_{AA}(r)}\right) \quad (1)$$

until the equilibrium RDFs ($g_i(r)$) of implicit water simulations match the RDFs obtained from atomistic simulations (within a small numerical error) for all ionic species (see Fig. S3). After each calculation of g(r), a moving average is applied to suppress statistical noise. An example of the generated NaCl coarse-grained potential for different salt concentrations is shown in Fig. S2. In our molecular dynamics simulations with implicit solvent, this short-range potential is always used in conjunction with the long-range Coulomb potential to reproduce full ion-solvent structures.

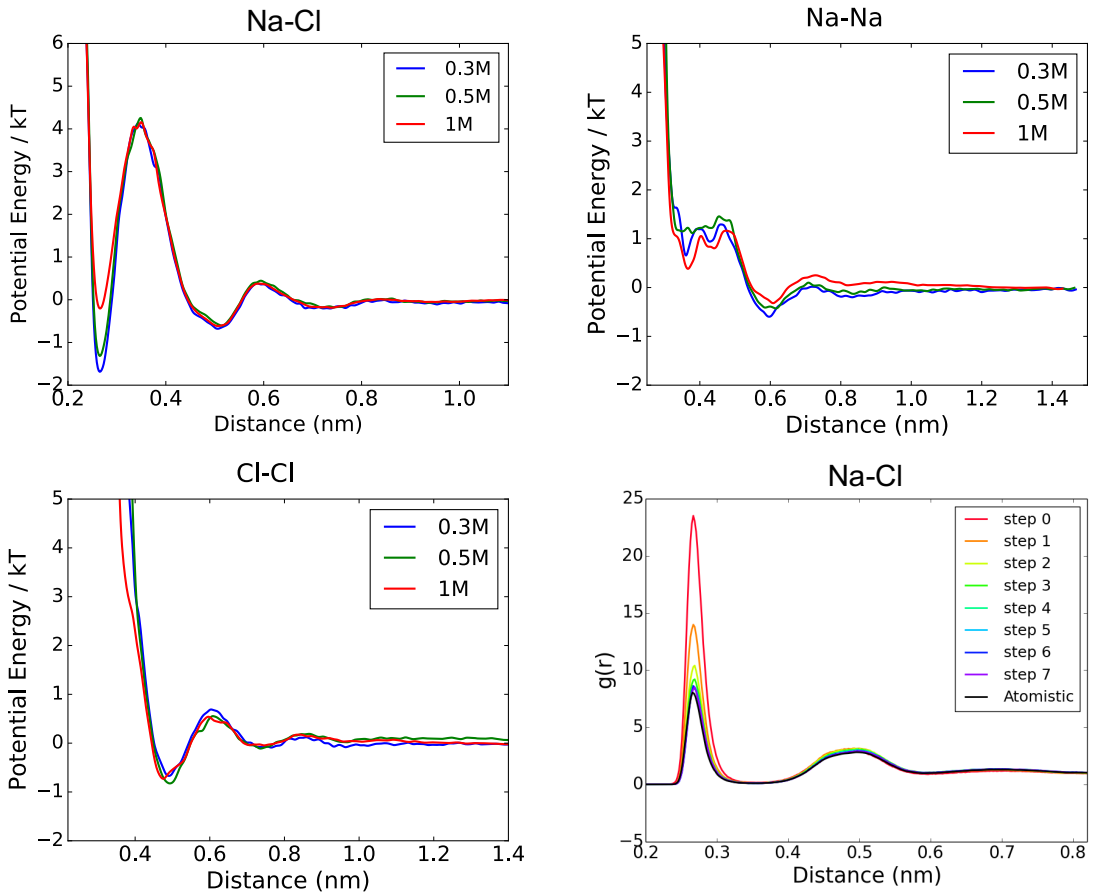

Fig. S3. (a)-(c): Coarse-grained ion potentials calculated from atomistic radial distribution functions. The potentials demonstrate multiple energy minima due to solvation effects. (d) Demonstration of the evolution of pair-correlation function (g(r)) during the process of Iterative Boltzmann Inversion. Only the g(r) between Na ions and Cl ions are shown, the other two pairs (Na-Na and Cl-Cl) are similar.

3. Details of Coarse-grained Simulations

3. 1 Simple Smooth NPs

To study NP-NP interactions, two nanoparticles are fixed symmetrically along the long axis of a tetragonal simulation box (See Fig. 2 in the main text for a snapshot, all simulation snapshots in the maintext and the SI Appendix are rendered using Visual Molecular Dynamics (4)). The total force on the two nanoparticles are recorded and averaged 1000 times in 450 ns at intervals of 450 ps. Average forces are recorded at 60 different NP-NP distances for each curve, and each simulation is performed 3 times with different randomly generated initial states. A spline fitting is employed to get smooth curves of mean forces, which are then used for numerical integration to get the effective potentials.

Coarse grained simulations use a set of SI units defined by length unit $D = 1\,\mathrm{nm}$, energy unit $\varepsilon = 1k_BT \approx 0.0257\mathrm{eV}$, and mass unit $M = 23.5\ \mathrm{u} \approx 3.9\times10^{-26}\mathrm{kg}$. All other units can be derived according

to the online documentation of HOOMD-blue (17). For example, time unit τ can be derived as $\tau = \sqrt{MD^2/\varepsilon} \approx 3\times10^{12}$s.

To avoid undesired boundary effects, coarse grained simulations for force measurement between NPs are performed in simulation boxes with dimensions of at least $16\times16\times32$ (nm^3). For highly charged NPs, considering the longer range of NP interactions and ion distribution profiles, the box size is increased to $20\times20\times40$. Simulation results remain the same when we further increase the box size, suggesting that the simulation boxes are sufficiently large.

Table 1 Parameters used in simple sphere NP simulations. Plots in Fig. 1 and Fig. 2 (main text) are simulated using values in the middle column. The softness of NP is set to be comparable to ion size by setting ε to a small value or σ to be the mean hydrated ion size.

ε (kT)	1.0	0.001	0.001
σ (nm)	0.6	1.0	1.0

Table 2 Size of particles used in simple sphere NP simulations.

Type of Beads	Na	Cl	NP
R (nm)	0.15	0.22	4

As mentioned in the main text, the shifted Weeks-Chandler-Anderson (WCA) potential is used for the ion-NP interactions: $V_{WCA}(r) = 4\varepsilon[\left(\frac{\sigma}{r-\Delta}\right)^{12} - \left(\frac{\sigma}{r-\Delta}\right)^{6}]$. Δ is determined by the Lorentz combining rules (18): $\Delta_{ij} = R_i + R_j$. The values of σ, ε and R are given in Table 1 and Table 2. The radii of ions are estimated from the derived short-ranged potential by finding the distance at which the repulsion exceeds 5 kT (energy unit in the simulations). They are found to have minimal influence on the overall conclusions.

To make reasonable comparison with experimental parameter and hard-sphere depletion theories, the sizes of the NPs are estimated by the Barker-Henderson mean collision diameter (19):

$$d_{ab}^{BH}(\beta) = -\int_0^{\infty} \left(e^{-\beta u_{ab}(r)} - 1\right) dr$$

The diameter of NPs with repulsive WCA potentials is 8.7 nm for the middle column in Table 1, calculated from this equation. In all NP-NP potential curves, the rapid growing repulsion between 8.5 and 8.7 nm result from the WCA potential which represent the hard-core repulsion of the NPs.

In order to test the effectiveness of the calculated potential of mean force in many-body circumstances, we introduce a 3rd NP in our simulation so that three NPs form the vertices of an equilateral triangle. The total force and corresponding potential along one edge is shown in Fig. S4. Qualitative behavior of the effective force is maintained in the presence of multibody effect.

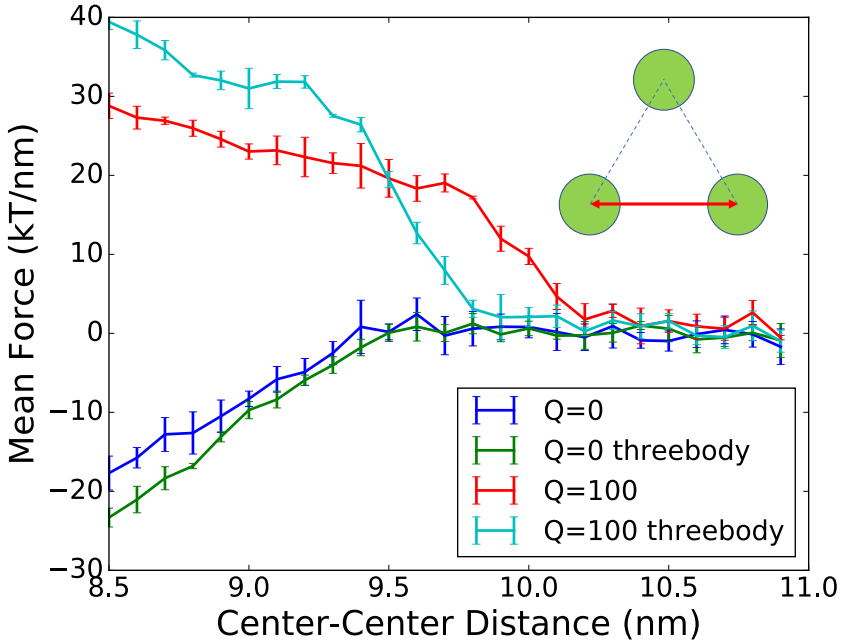

Fig. S4 Simulated mean force along lateral direction from 3 NPs forming the vertices of an equilateral triangle (as shown in the inset), compared with two NP calculations (blue and red curves). For neutral NPs, the lateral force in three body occasion is roughly 1.5 times the force between pairs of NP, which is the value one would get assuming the ion-induced force is linearly additive. For NPs with a large charge (in this case 100 elementary charges), the mean force in 3-body simulations is stronger at short distances but then decrease faster.

In this paper, we neglect the polarization charge on the NP-solvent interface, which can give a non-trivial contribution to the short-range association-dissociation of ions to the charged NPs. Since the aim of this paper is a general study of the interaction of nanometer-size particles, we omit the surface details of the particle-solvent interface, which are also short-range. Instead, we focus on the treatment of the long-range Coulombic force and how bulk ion-correlation influence NP-NP interactions.

3.2 DNA-grafted NPs

We use force fields derived from the models described in (20, 21) with a few modifications. A charge of -1 e is added to every base of the DNA strand. The intrinsic bending potential of dsDNA is multiplied by 2/3 to account for charge-induced rigidity, which is implicit in the bending potential in the previous model. The reduced energies used in previous models are converted to real units by assuming that T=1.5 (reduced temperature) in the previous model is equivalent to a temperature of 300K.

Short range interactions between ions and DNA were modeled by a simple shifted WCA potential similar to other excluded volume interactions in this paper. The range is set to the geometric mean between the bare ion radius and the DNA radius. The DNA strands possesses “sticky ends” that are not complementary with each other and are not charged (the charge is set on the ssDNA backbone). The flanking beads do not interact with ions. Box dimensions are set to 60 $c^{-1/3}$ nm, where c is the molar

concentration. An additional 40 nm is added in the z direction. The largest box used (at 0.3 M) is thus 90 nm × 90 nm ×130 nm.

Charged interactions are treated using a force-shifted Wolf summation with a cutoff of 4 nm, leading to 150 – 350 average neighbors in the force calculation. The calculation was ran using HOOMD-blue (17, 22) on 4 K80 GPUs over 7 – 15 days. Each potential of mean force is calculated using 300 points over the range 28-40 nm. The curves are numerically integrated using a trapezoidal integration rule and then fitted to Yukawa-type potentials. An extra generalized sigmoid function is added for 700 mM, low DNA density case. Typical fit results are shown on Fig. S5.

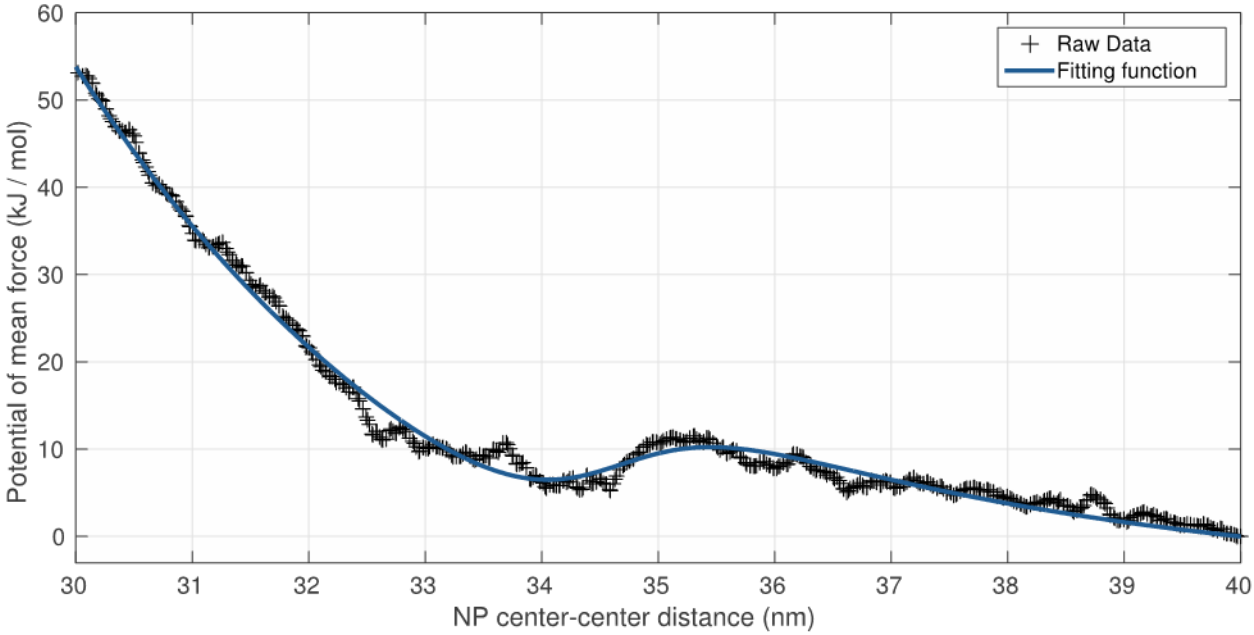

Fig. S5. Fit of the potential of mean force for a low grafting density at a concentration of 700 mM. The fitting function is described by the sum of a Yukawa-type potential ($a\ \mathrm{Exp}(-k\ r)\ /\ r$), where a and k are parameters and a generalized sigmoid in the form $f(r)\ =\ A\ (\ 1\ -\ 1\ /\ (1\ +\ \mathrm{Exp}(-\ K\ (r\ -\ r_0))))$, where A, K and r_0 are fitting parameters. Since the potential is obtained by direct integration, the fitting accounts for setting the potential to 0 at r = 40 nm. This is then shifted so that the potential of mean force vanishes at $r = \infty$.

We note that the DNA model in this work is overly simplistic in nature since the charges on DNA strands are not located at the center of the cylinder but rather close to the exterior. As such, realistic models would produce different ion condensation (23). Therefore, different interactions between nanoparticles are expected to appear in the strong overlap regime (d < 35 nm), while the behavior for large separations (d > 37 nm) should be similar.

4. Additional Results for Nanoparticle interactions

MD simulations are also performed at other NaCl concentrations and NP charge densities to see the transition from attraction to repulsion upon increasing surface charge of nanoparticles (NPs). At 1 M, the NP potential of mean force is similar to the 0.5 M NaCl case discussed in the main text, though the transition from attractive to repulsive occurs at a different charge density (Fig. S6). At both 1 M and 0.5

M, the transitions from attraction to repulsion appear to be abrupt, suggesting that the change in ion distribution has a non-linear effect on NP interactions.

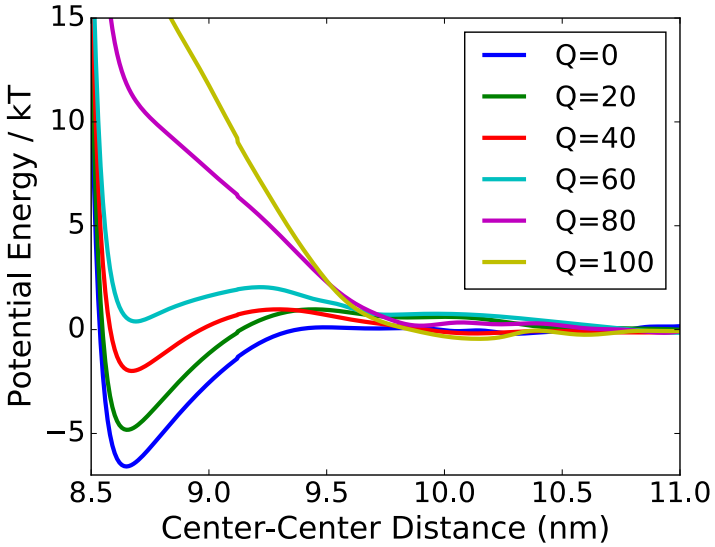

Fig. S6 NP-NP effective potential at 1M NaCl concentration. Similar to Fig. 2 in the main text, van der Waals attractions between are not included in order to specifically analyze the interaction due to ion correlations. A repulsive WCA potential is included, giving the repulsion at 8~8.7 nm.

Differences between the interactions of positively charged NPs and negatively charged NPs were studied by comparing selected sets of salt concentrations and surface charge densities (Fig. S7). We reported asymmetric behavior of positively and negatively charged NPs due to the size asymmetry of monovalent salt in an earlier paper (24). At equivalent surface charge density in ref (24), potentials for positively charged NPs are generally higher than the corresponding potentials for negatively charged particles, meaning the repulsion for positively charged NPs are stronger. This is because chloride ions are larger than sodium ions in the primitive model. In this work, we again note differences for NP charges with different signs; however, the difference is subtler because of the more complicated short-range interactions. Na^+ ions have a smaller hard-core radius than Cl^- ions, but due to the complicated shape of the coarse-grained ion potentials, there is no simple answer to which one of the ions is larger. However, in general, for intermediate surface charge density (for example, 0.3~2 e/nm^2 or 80<Q<500 for 1M NaCl concentration), repulsion is stronger for positively charged NPs.

NPs with very high surface charge densities (such as DNA grafted NPs) show different interaction trends compared with moderately charged NPs, as shown in Fig. S6. At 0.5 M NaCl, highly negatively charged NPs (over 500 e/NP or 2.1 e/nm^2) can lead to a long-range attractive well ~1.5-2 nm from the surface (corresponding to a center-center distance of ~10-10.5 nm, given that the NP diameter is ~8.7 nm). These were not observed for positively charged NPs. At 1 M NaCl, shallow potential wells are observed for both positively and negatively charged NPs.

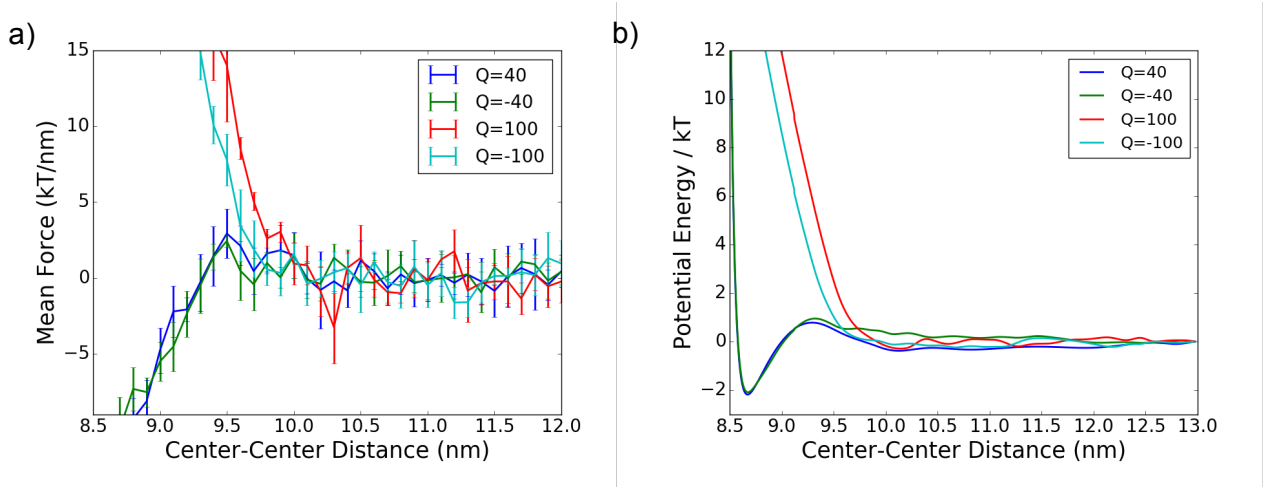

Fig. S7. a) Mean force and b) effective potential for positively and negatively charged NPs at 0.5 M NaCl.

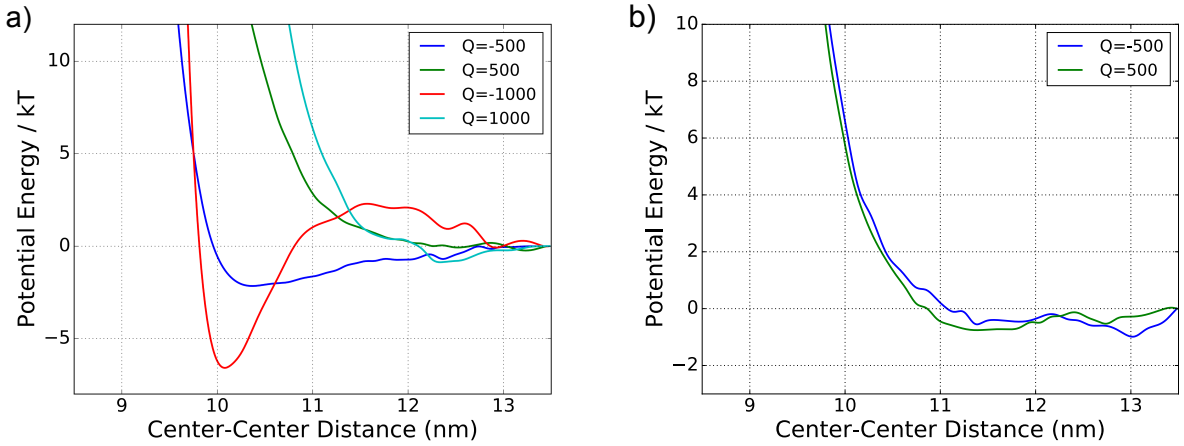

Fig. S8. Effective potentials between highly charged NPs at (a) 0.5 M NaCl and b) 1M. At 0.5 M, long-range attractive wells occur 1.5 nm away from the NP surface for negatively charged NPs, but not for positively charged NPs. At 1 M, both positively and negatively NPs show shallow but long-range attractive wells.

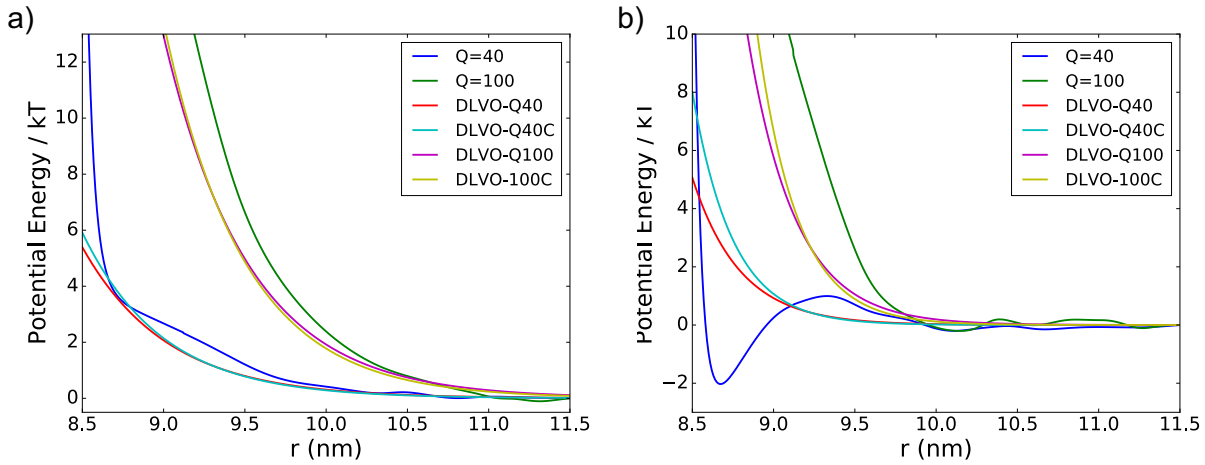

Fig. S9. Comparison of simulated effective potentials between two NPs at salt concentrations of (A) 0.3 M and (B) 1 M with DLVO theory, and DLVO theory with corrected dielectric constants that depends on ion concentration (denoted in the labels by DLVO-Q40C and DLVO-Q100C). The numbers following Q indicate the total charge on each NP, in the unit of elementary charges. All of the curves are plotted without van der Waals attraction. At intermediate concencentrations (such as 0.3M), DLVO theory gives a reasonable match to simulations, slightly underestimating the repulsion. At high concentrations, the DLVO theory deviates from simulation results for both low-charge and high-charge NPs.

We also compare the effective potentials with the widely used screened electrostatic potential in DLVO theory,

$$\beta U(r) = Z^2 l_B \left(\frac{e^{\kappa a}}{1+\kappa a}\right)^2 \frac{e^{-\kappa r}}{r} \qquad (2)$$

to study how the interaction deviates from mean field approaches (Fig. S9). The radius a on the right-hand side of equation (2) is taken to be the distance at which ion-NP RDF rise from zero to finite values, i.e. 4.6 nm. As already pointed out in earlier works (24, 25), DLVO theory underestimates the interaction strength, because it sees charges as a mean field of point charges that have no short-range interactions, and thus neglecting sophisticated ion correlations. At higher ion concentrations (1M), the deviation is more significant. Moreover, DLVO theory predicts no NP-NP effective attraction from ions, such as depletion attractions. We also show in Fig. S9 that DLVO theory, even with the correction of dielectric permittivity as a function of ion concentration, fails to explain the strong repulsions for charged NPs in concentrated electrolyte. As dielectric constant decreases, the Bjerrum length increases leading to a larger pre-factor in the potential, but Debye length ($\lambda_D = 1/\kappa$) decreases. The overall effect is that the range of repulsion is shorter if the dielectric constant decreases. Therefore, corrections in dielectric permittivity cannot explain the strong and long-range repulsion. At high salt concentrations, interactions between charged NPs are dominated by ion correlations, which makes the potentials differ from the screened Coulomb potential both in strength and functional forms.

To analyze the correlation length in our model NaCl systems, we extract the characteristic length by finding and fitting the peaks of Na-Cl pair correlation functions at different concentrations. In the full atom simulations an increase in the ion-ion correlation associated screening length in bulk NaCl at high salt concentration is not observed maybe due to finite size effects but it is observed in the coarse grained

simulations. For comparison of the different models to our results, in Fig. S10 we also plotted the corrected classical Debye-Huckel (CDH), the corrected Debye-Huckel Bjerrum (26) (CDHBj) screening length by including the decrease of the water dielectric constant with increasing salt concentration in the DH and DHBj models. Allowing the formation of Bjerrum pairs in the DHBj model reduces screening; that is, increases the screening length. The CDHBj theory does predict a longer screening length than the CDH theory. However, it is also larger than the associated screening length obtained by our atomistic simulations. This is probably due to 1) excluded volume effects, which becomes more important as the concentration increases (as shown in our model and in Fig 3 of ref (26) when the hard core is included, i.e. the DHBjDIHC curve), and 2) the contribution of the larger than binary ion clusters to screening, which is known to give a very different contribution to the free energy than the DH model (see for example the contribution of polymers with ion (27) or without ion association (28). A few models, including one based on the Ornstein-Zernike equation (29) and restricted primitive model (30, 31), predict an absolute increase of the value of the bulk screening length when extrapolated to high salt concentrations. An increase in the screening length is observed by carefully fitting the exponential decay length in the g(r) calculated up to 3 nm from 48 thousand frames taken over 48 million MD steps of coarse-grained ion simulations (see Fig. S10 b). Error bars are obtained from the 95% confidence interval. Adjusted Pearson correlation coefficients for this procedure are around $r^2 \sim 0.85$. This increase has been observed in confinement (on mica surfaces (32) and in capacitance studies (33, 34)) when fitting an exponential decay at high salt concentrations, in agreement with our results on DNA-functionalized NPs which have an effective radius much larger than the NPs with smooth surfaces, suggesting that confinement may be responsible for the observed increase.

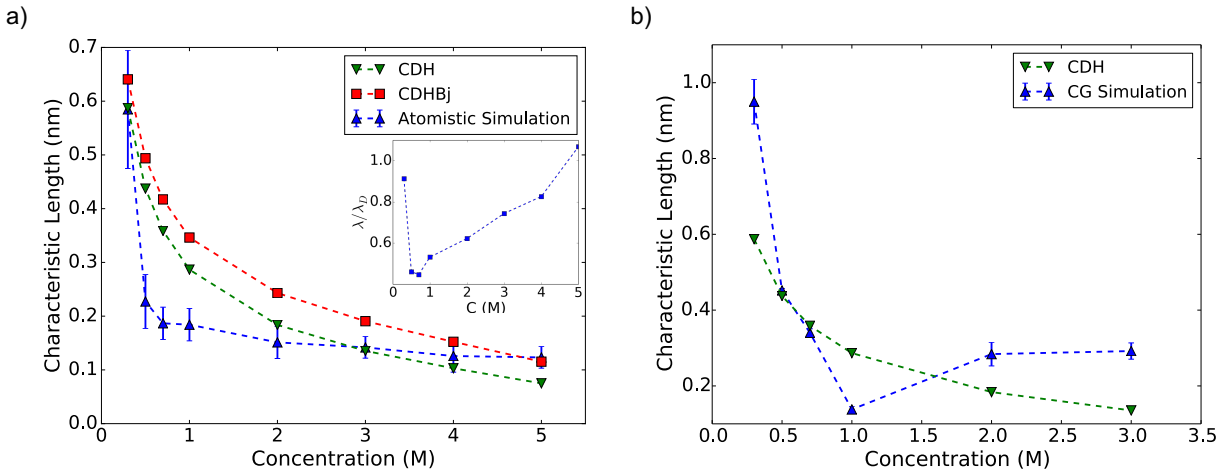

Fig. S10 Comparison of screening length obtained from simulations (up triangles), Debye-Huckel theory with concentration dependent dielectric constant (CDH, down triangles), and Debye-Huckel Bjerrum theory with concentration dependent dielectric constant (CDHBj, red squares). a) The correlation length obtained from fitting the first 4 peaks of g(r) from atomistic simulations is smaller than the Debye-Huckel screening length. CDHBj theory predicts a higher screening length due to the formation of Bjerrum pairs. Inset: The ratio of the simulation correlation length (λ) to the corrected DH length (λ_D) versus concentration. b) Comparison of CDH theory (down triangles) and the screening length obtained by fitting the exponential tail of pair correlation function obtained from coarse-grained simulation of ions.

5. Short-chain Polymer Simulations

Polymers without specific interactions with NPs have been known to lead to depletion attractions between NPs or proteins, and thus cause crystallization or gelation (35-37). To illustrate the similarity between depletion induced by ion correlation and depletion interactions in polymer solutions, MD simulations of NPs immersed in a polymer solution are performed with similar geometry as the NaCl simulations. Polymers of 8-32 segments are modeled as bead-spring chains with repulsive Lenard-Jones potentials,

$$U_{ij}(r) = 4\varepsilon\left[\left(\frac{\sigma}{r-\Delta}\right)^{12} - \left(\frac{\sigma}{r-\Delta}\right)^{6}\right] + \delta$$

where each bead represents one segment. A cutoff radius of $r = 2^{1/6}\,\sigma$ is set so that only the repulsive part of LJ potential is preserved. To relate the two systems, $\sigma = 1$ nm and $\Delta = 8$ nm for bead-NP interactions and 0 for bead-bead interactions. Harmonic bonding is used to connect consecutive polymer segments:

$$U_b(r) = \frac{1}{2}k(r-\sigma)^2$$

with an elastic constant $k = 330 k_B\,T/\mathrm{nm}^2$. A constant temperature of 298 K is maintained by Langevin dynamics, and periodic boundary conditions are applied in 3 directions.

The RDF between the monomer beads are shown in Fig. S12. The RDF of the monomer beads share a lot of similarities to the RDF between sodium and chloride ions in Fig. S3, suggesting a similar underlying mechanism of depletion interaction induced by polymer and correlated ion clusters.

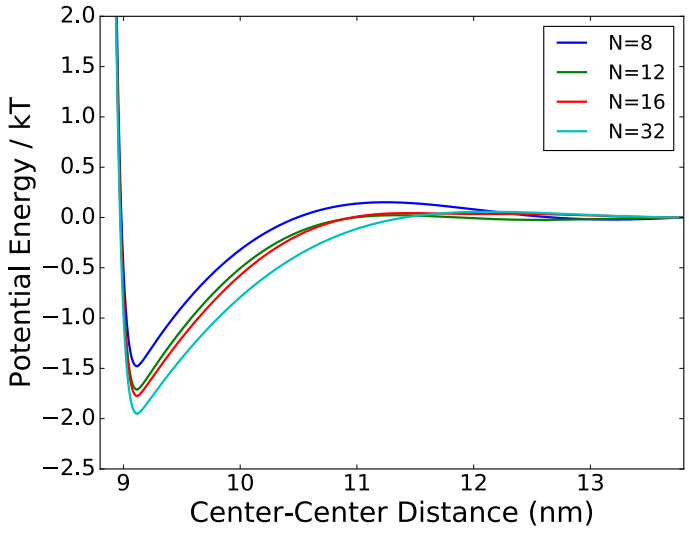

Fig. S11. Inter-NP interactions for neutral NPs with depletion induced by neutral short-chain polymers. NPs are 9 nm in diameter. N denotes the number of segments in each polymer chain. The polymer volume fraction is fixed at 0.1. For the length regime in our studies, the depletion potential depth and range increases monotonically with chain length. The interaction range is similar to the correlation length (plotted in Fig. S12) rather than given by twice the radius of gyration.

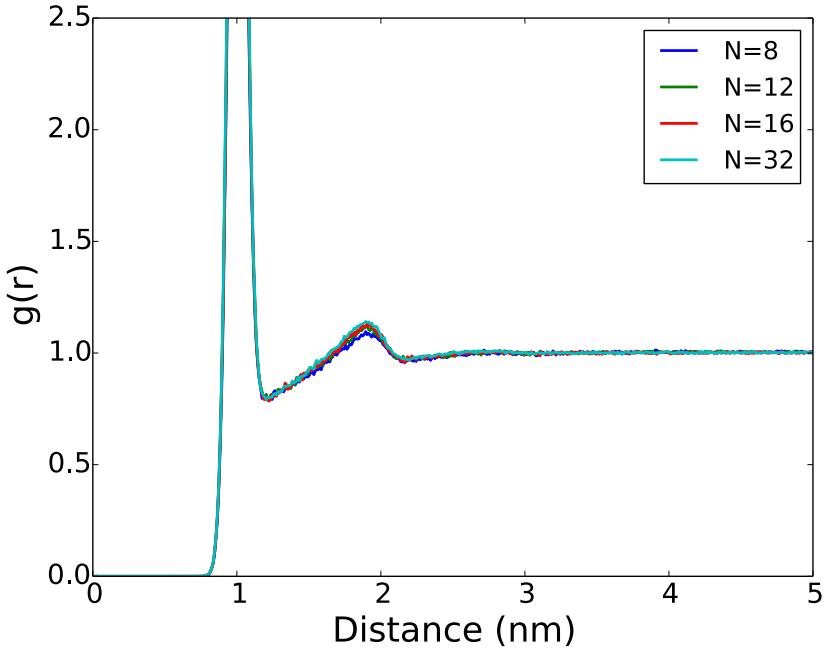

Fig. S12 Radial distribution function (RDF) of polymer beads. The oscillation in the RDF is a result of competition of packing effects and chain correlations. For longer chains, the 2nd correlation peak is more pronounced, giving rise to stronger depletion interactions.

6. Ion Distributions and Cluster Analysis

In order to analyze the relationship between NP interactions, ion distribution and ion clustering analysis are performed. The distribution of ions around a single NP is performed with the radial distribution function extension of VMD (4), using an isolated NP immersed in NaCl ions. The MD simulation parameters and ion interaction potentials were identical with those used in simulations of effective interactions. Fig. S13 shows that, as expected, a peak of counterions (chloride ions) and a depleted layer of coions show up near the NP surface. The thickness of this layer is about 1 nm, corresponding to the NP interaction range in the low and intermediate surface charge density regime. There is also a difference between the distributions of the two types of ions around a neutral NP, because of the asymmetry in ion steric effects (38). The depleted layer of coions and an amplified layer of counterions coexist near the NPs, which leads to a complicated competition between depletion attraction and repulsion due to the aggregation of ions around NPs.

Cluster analysis was described briefly in the Methods in the main text. The analysis benefited from the established code in ref (39). r_{cut} is chosen to include the second most significant peak in the Na-Cl RDF, which is 0.59 nm. To facilitate the analysis, the simulation box is divided into small cubic cells of 0.5 nm. The spatial distribution of ion clusters in each cell is analyzed by long-time averaging. For example, the distributions of Bjerrum pairs, ion trimers and tetramers averaged in a 4.5 nm slab cutting through the box and the two NPs are shown in Fig. S15. The distance between the two NPs is 9.1 nm, which should leave a large enough gap for single ions. A region of low cluster concentration can be

identified that has a radius larger than $R + r_{ion}$, which is the common excluded volume radius for hard spheres. Moreover, the gap between two NPs is also depleted in cluster concentration. For larger clusters, the size of the depleted gap between the two NPs are larger (i.e. trimer>dimer>monomer), which means that larger clusters have a stronger contribution to depletion attraction. The spatial distribution of ion clusters confirm that there is indeed a depletion in cluster concentration near NP surfaces that could facilitate longer-ranged depletion attraction.

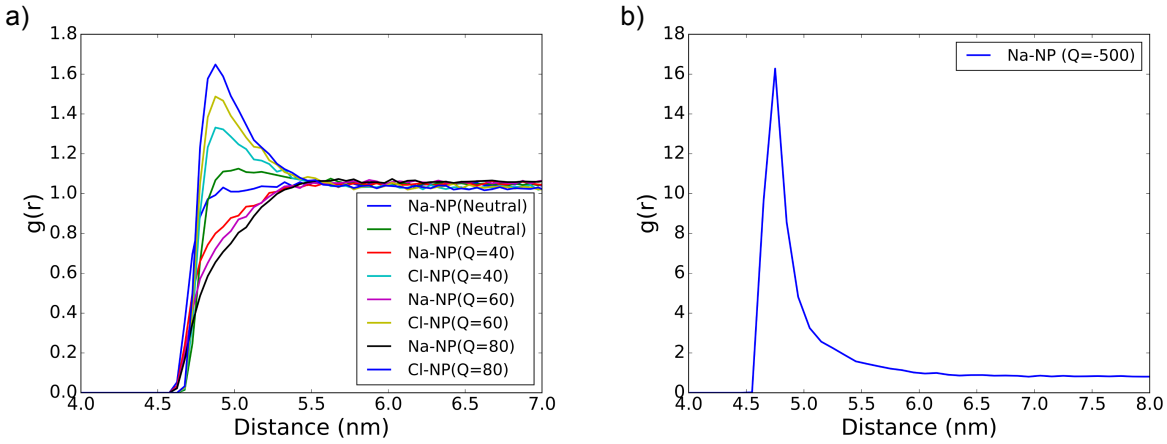

Fig. S13. a) Distribution of ions around isolated NPs. The numbers such as Q=40 indicates the total surface charge on the NP, in the unit of elementary charge. The distribution of counterions for a very highly charged NP in 0.5 M NaCl is shown separately in (b). b) The exceptionally high peak corresponds to the counterion condensation as is visually obvious in the simulation snapshot in Fig. S14.

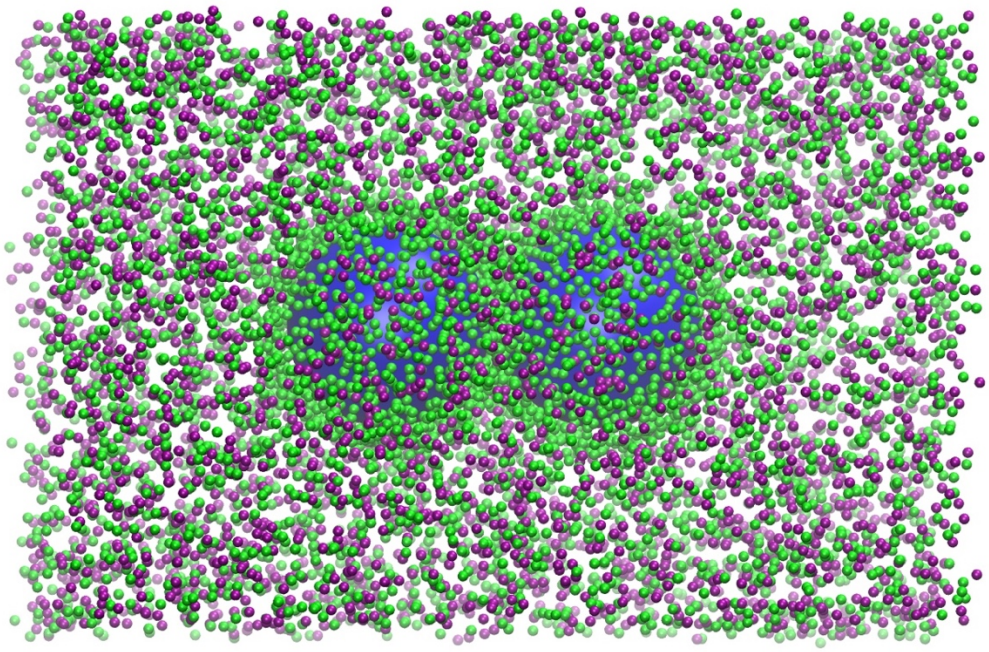

Fig. S14. Simulation snapshot of highly positively charged NP (500 e per np) interaction in 0.5 M NaCl. Green beads indicate chloride ions, purple bead indicate sodium ions. The snapshot shows strong counterion condensation on the NP surface at sufficiently high surface charge densities.

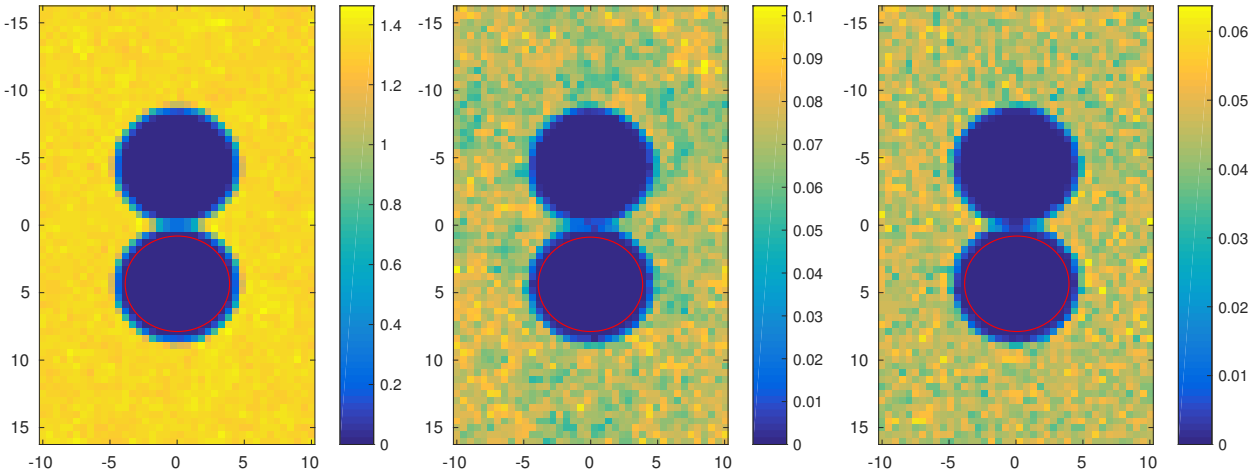

Fig. S15 Spatial distribution of ions and ion clusters of NP with intermediate charge (60 e per particle): a) free ions, b) Bjerrum pairs and c) trimers. The numbers on the axes represent length with a unit of nm, the colorbar indicates averaged probability of finding free ions, pairs, etc., in arbitrary unit. Depleted regions (light blue) are observed around the NPs and the gap between them. For larger clusters (b and c), both the depleted sphere radius and the depleted gap between NPs are larger. The red circle indicate the hard-core diameter of the NPs.

1. Darden T, York D, & Pedersen L (1993) Particle mesh Ewald: An N· log (N) method for Ewald sums in large systems. *The Journal of chemical physics* 98(12):10089-10092.
2. Phillips JC*, et al.* (2005) Scalable molecular dynamics with NAMD. *J. Comput. Chem.* 26(16):1781-1802.
3. Hess B, Kutzner C, Van Der Spoel D, & Lindahl E (2008) GROMACS 4: algorithms for highly efficient, load-balanced, and scalable molecular simulation. *Journal of chemical theory and computation* 4(3):435-447.
4. Humphrey W, Dalke A, & Schulten K (1996) VMD: visual molecular dynamics. *Journal of molecular graphics* 14(1):33-38.
5. Jorgensen WL, Chandrasekhar J, Madura JD, Impey RW, & Klein ML (1983) Comparison of simple potential functions for simulating liquid water. *The Journal of chemical physics* 79(2):926-935.
6. Luo Y & Roux B (2009) Simulation of osmotic pressure in concentrated aqueous salt solutions. *The Journal of Physical Chemistry Letters* 1(1):183-189.
7. Berendsen H, Grigera J, & Straatsma T (1987) The missing term in effective pair potentials. *J. phys. Chem* 91(24):6269-6271.
8. Weerasinghe S & Smith PE (2003) A Kirkwood–Buff derived force field for sodium chloride in water. *The Journal of chemical physics* 119(21):11342-11349.
9. Shen J-W, Li C, van der Vegt NF, & Peter C (2011) Transferability of coarse grained potentials: Implicit solvent models for hydrated ions. *Journal of Chemical Theory and Computation* 7(6):1916-1927.
10. Neumann M, Steinhauser O, & Pawley GS (1984) Consistent calculation of the static and frequency-dependent dielectric constant in computer simulations. *Molecular Physics* 52(1):97-113.
11. Reddy MR & Berkowitz M (1989) The dielectric constant of SPC/E water. *Chemical Physics Letters* 155(2):173-176.
12. van der Spoel D, van Maaren PJ, & Berendsen HJ (1998) A systematic study of water models for molecular simulation: derivation of water models optimized for use with a reaction field. *The Journal of chemical physics* 108(24):10220-10230.
13. Lyubartsev AP & Laaksonen A (1995) Calculation of effective interaction potentials from radial distribution functions: A reverse Monte Carlo approach. *Physical Review E* 52(4):3730-3737.
14. Hess B, Holm C, & van der Vegt N (2006) Modeling multibody effects in ionic solutions with a concentration dependent dielectric permittivity. *Physical review letters* 96(14):147801.
15. Soper A (1996) Empirical potential Monte Carlo simulation of fluid structure. *Chemical Physics* 202(2-3):295-306.
16. LeBard DN*, et al.* (2012) Self-assembly of coarse-grained ionic surfactants accelerated by graphics processing units. *Soft Matter* 8(8):2385-2397.
17. Anderson JA, Lorenz CD, & Travesset A (2008) General purpose molecular dynamics simulations fully implemented on graphics processing units. *Journal of Computational Physics* 227(10):5342-5359.
18. Lorentz H (1881) Ueber die Anwendung des Satzes vom Virial in der kinetischen Theorie der Gase. *Annalen der physik* 248(1):127-136.
19. Hansen J-P & McDonald IR (1990) *Theory of simple liquids* (Elsevier).
20. Li TI, Sknepnek R, Macfarlane RJ, Mirkin CA, & Olvera de la Cruz M (2012) Modeling the crystallization of spherical nucleic acid nanoparticle conjugates with molecular dynamics simulations. *Nano letters* 12(5):2509-2514.

21. Knorowski C, Burleigh S, & Travesset A (2011) Dynamics and statics of DNA-programmable nanoparticle self-assembly and crystallization. *Physical Review Letters* 106(21):215501.
22. Glaser J*, et al.* (2015) Strong scaling of general-purpose molecular dynamics simulations on GPUs. *Computer Physics Communications* 192:97-107.
23. Hinckley DM & de Pablo JJ (2015) Coarse-grained ions for nucleic acid modeling. *Journal of chemical theory and computation* 11(11):5436-5446.
24. Guerrero-García GI, González-Mozuelos P, & de la Cruz MO (2011) Potential of mean force between identical charged nanoparticles immersed in a size-asymmetric monovalent electrolyte. *The Journal of chemical physics* 135(16):164705.
25. Boström M, Williams D, & Ninham B (2001) Specific ion effects: why DLVO theory fails for biology and colloid systems. *Physical Review Letters* 87(16):168103.
26. Fisher ME & Levin Y (1993) Criticality in ionic fluids: Debye-Hückel theory, Bjerrum, and beyond. *Physical review letters* 71(23):3826.
27. De La Cruz MO*, et al.* (1995) Precipitation of highly charged polyelectrolyte solutions in the presence of multivalent salts. *The Journal of chemical physics* 103(13):5781-5791.
28. Borue VY & Erukhimovich IY (1988) A statistical theory of weakly charged polyelectrolytes: fluctuations, equation of state and microphase separation. *Macromolecules* 21(11):3240-3249.
29. Attard P (1993) Asymptotic analysis of primitive model electrolytes and the electrical double layer. *Physical Review E* 48(5):3604.
30. Ennis J, Kjellander R, & Mitchell DJ (1995) Dressed ion theory for bulk symmetric electrolytes in the restricted primitive model. *The Journal of chemical physics* 102(2):975-991.
31. González-Mozuelos P, Yeom M, & de la Cruz MO (2005) Molecular multivalent electrolytes: microstructure and screening lengths. *The European Physical Journal E* 16(2):167-178.
32. Smith AM, Lee AA, & Perkin S (2016) The electrostatic screening length in concentrated electrolytes increases with concentration. *The journal of physical chemistry letters* 7(12):2157-2163.
33. Limmer DT (2015) Interfacial ordering and accompanying divergent capacitance at ionic liquid-metal interfaces. *Physical review letters* 115(25):256102.
34. Uralcan B, Aksay IA, Debenedetti PG, & Limmer DT (2016) Concentration Fluctuations and Capacitive Response in Dense Ionic Solutions. *The journal of physical chemistry letters* 7(13):2333-2338.
35. Lu PJ*, et al.* (2008) Gelation of particles with short-range attraction. *Nature* 453(7194):499-503.
36. De Hoog E, Kegel W, Van Blaaderen A, & Lekkerkerker H (2001) Direct observation of crystallization and aggregation in a phase-separating colloid-polymer suspension. *Physical Review E* 64(2):021407.
37. McPherson A (1976) Crystallization of proteins from polyethylene glycol. *Journal of Biological Chemistry* 251(20):6300-6303.
38. Jing Y, Jadhao V, Zwanikken JW, & Olvera de la Cruz M (2015) Ionic structure in liquids confined by dielectric interfaces. *The Journal of chemical physics* 143(19):194508.
39. Nguyen TD, Schultz BA, Kotov NA, & Glotzer SC (2015) Generic, phenomenological, on-the-fly renormalized repulsion model for self-limited organization of terminal supraparticle assemblies. *Proceedings of the National Academy of Sciences* 112(25):E3161-E3168.